Structural, electrical, optical and phase investigation of perovskite barium zirconate (BaZrO$_3$) nanoparticles prepared through auto-combustion technique

J. Abimalar[1,2], V. Anslin Ferby[1,2]

[1]Department of Physics and Research Centre, Scott Christian College (Autonomous), Nagercoil – 629 003, Tamil Nadu, India

[2]Manonmaniam Sundaranar University, Abishekapatti, Tirunelveli – 627 012, Tamil Nadu, India

Corresponding author: J. Abimalar, jabimalar98@gmail.com

ABSTRACT The BaZrO$_3$ ceramics were prepared via sol-gel auto-combustion technique with three Fuel to Oxidant (F/O) ratios ($\varphi = 0.5$, 1.0 and 1.5) and annealed at 1200 °C for 2 hours. X-ray diffraction (XRD) and Rietveld refinement data confirmed the cubic perovskite phase with the Pm$\bar{3}$m (221) space group. These three samples are well indexed in JCPDS no: 06-0399. The ratio $F/O = 1.0$ gives one a small crystallite size and very high surface area. The ratio $F/O = 1.5$ provides a very high crystallite size and very low dislocation density. The oxygen vacancies in the samples were analyzed using Raman spectroscopy. The optical band gap energy value increases from 2.02 to 3.09 eV with increasing F/O ratio. Using of impedance spectroscopy for BaZrO$_3$ at room temperature allows us to reveal decreasing Ionic conductivity with an increasing F/O ratio. The Nyquist plot for all samples exhibits a circular arc in the high-frequency zone and nearly a straight line in the low-frequency region. Due to the presence of low grain boundary with high ionic conductivity the BaZrO$_3$ electrolyte material is used for energy storage in devices.

KEYWORDS nanoparticle, combustion synthesis, X-ray diffraction technique, Rietveld refinement analysis, FT-Raman spectroscopy, UV-vis absorption spectrum, impedance

FOR CITATION Abimalar J., Anslin Ferby V. Structural, electrical, optical and phase investigation of perovskite barium zirconate (BaZrO$_3$) nanoparticles prepared through auto-combustion technique. *Nanosystems: Phys. Chem. Math.*, 2023, **14** (4), 467–478.

1. Introduction

BaZrO$_3$ is a cubic perovskite with a structure ABO$_3$. Because of its unusual physical properties, BaZrO$_3$ is attractive for usage in electro-ceramics [1]. BaZrO$_3$ (BZO) is an ideal model for a wide range of ABO$_3$ perovskite. They have different technical applications, including high-temperature materials, electronic ceramics, nonlinear optics, catalysis, superconductors, etc. [2–7]. Barium Zirconate is an alkaline earth perovskite with significant electro-ceramic potential [8–10]. High proton conductivity and green-blue emission are the advantages of a structurally disordered vacancy in the BaZrO$_3$ semiconductor [8, 11].

The perovskite materials are used for capacitors, nonvolatile memory, actuators, sensors, piezoelectric, ultrasonic, underwater devices, high-temperature heating applications, frequency filters for wireless communications, and other applications [12–15]. Barium zirconate (BaZrO$_3$) has significant economic and technological importance because of its properties such as a "high melting point (2920 °C), poor thermal conductivity, remarkable mechanical and structural integrity under intense heat conditions, strong protonic conductivity, etc. [12–17]". BaZrO$_3$ is a photoluminescence (PL) material with low cost and good environmental performance that emits light in the visible spectrum [18]. BaZrO$_3$ ceramics also have exceptional dielectric characteristics, making them a good choice for microwave and wireless communication applications [9, 10]. BaZrO$_3$ can be formed by several methods: hydrothermal [20], ceramic [21], co-precipitation [22], etc.

Advanced ceramics, catalysts, and nanomaterials are prepared by a simple and practical combustion synthesis process [23]. Based on the propellant chemistry concepts used in this technique [24], a redox reaction involves the interaction of an oxidant and a fuel. Various types of combustion synthesis differ mainly in the reactants or burning method [23, 25–29]. For comparison, conventional techniques like solid-state synthesis and combustion-based methods, nitrate methods may generate monophasic nanopowders with homogeneous microstructure at lower temperatures or faster reaction times [30–33]. A commonly used solution combustion process is called citrate-nitrate auto-combustion synthesis (CNA) [34–36]. Metal nitrates are used as oxidants, and citric acid as fuel. The well-known Pechini approach and the CNA method are similar in many ways [37, 38]. "Sol-gel combustion method" is more efficient [39]. However, the CNA approach varies from the Pechini process in which the nitrates are not first removed as NO$_x$ but remain with the metal citrates that ignite the auto-combustion.

BaZrO$_3$ nanoparticles obey good electrical properties and high ionic conductivity. Nowadays researchers are mainly focused on developing energy storage devices. To enhance the efficiency of materials, researchers are working on combining transition metal oxides (TMOs) with other transition metals, metal oxides, ABO$_3$ or BO$_2$-type materials, etc. These materials can modify the surface area, pore characteristics, ion intercalation/ deintercalation, conductivity etc. TMO is an efficient electrode material, especially in supercapacitors and solar cell applications. Peng-Jian Wang et al. worked with BaTiO$_3$–Bi(Li$_{0.5}$Nb$_{0.5}$)O$_3$ nanocomposites. From the result, the maximum energy density obtained is 14.2 J/cm^3 at 497 mv/m. This simple filler preparation method provides a universal and best technical approach for high energy density capacitors. It is the successful application of universal nanocomposites [40]. Recently, hexaferrites reported to possess a spontaneous electrical polarization at room temperature [41].

In this research work, citric acid is chosen as fuel, because it has good complexing ability, low ignition temperature (200 – 250 °C) and controlled combustion reaction with nitrates. In this paper, the synthesis and characterization of BaZrO$_3$ nanoparticles with various F/O ratios through the "sol-gel auto-combustion method" was reported.

2. Experimental procedure

2.1. Synthesis of BaZrO$_3$ nanoparticles

Citric acid (C$_6$H$_8$O$_7$) was chosen as the fuel, and Ba(NO$_3$)$_2$ (barium nitrate) and ZrO(NO$_3$)$_2 \cdot x$H$_2$O (zirconium (IV) oxynitrate hydrate) were used as sources of cations and oxidants [42]. Gravimetric analysis revealed that ZrO(NO$_3$)$_2 \cdot x$H$_2$O has a hydration level (x) of 1. Metal–Nitrate solution prepared by dissolving stoichiometric weighed Ba(NO$_3$)$_2$ and ZrO(NO$_3$)$_2 \cdot x$H$_2$O separately in deionized water. This stage gave rise to a clear solution indicating total dissolution. NH$_4$OH was added drop by drop and adjusted the pH 7 using a pH meter. After heating the combination of ammonia and the neutralized solution to 80 °C on a hot plate and continuously stirring, the two components evaporated to dryness. The solution became more viscous as the water evaporated, forming the extremely viscous gel. The gel ignited temperature raised to 100 – 120 °C. The dried gel burned to create a soft powder. The following equation represents the combustion reaction:

$$9Ba(NO_3)_2 + 9ZrO(NO_3)_2 \cdot xH_2O + 10C_6H_8O_7 \longrightarrow 9BaZrO_3 + 49H_2O + 60CO_2 + 18N_2. \tag{1}$$
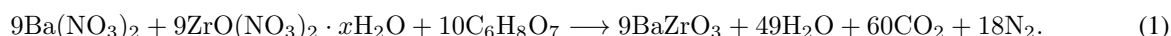
For the formation of phase pure Barium Zirconate nanoparticles, the following procedure is used. The resultant ash powder is dried and crushed for annealing purposes. 'Indfurr furnaces' were used for annealing. Time profile controllers will allow the feed to a set 1200 °C temperature and hold for two hours at the particular setting temperature. The heating and cooling rate is 10 °C/min and the annealing temperature is 1200 °C. It helps us to reduce the secondary phase of BaCO$_3$.

Lattice constant is obtained by the following equation

$$\frac{1}{d_{hkl}^2} = \frac{h^2 + k^2 + l^2}{a^2}. \tag{2}$$

The average lattice constant, determined using the previously mentioned calculation, is $a = 4.17$ Å. This estimated lattice constant value agrees well with the reference data, $a = 4.19$ Å [43].

Applying Scherer's formula, the full width at half maximum (FWHM) of the high-intensity peak (110) is used to calculate the crystallite size:

$$D = \frac{k\lambda}{\beta \cos \theta}, \tag{3}$$

where D denotes the crystallite size in nanometres, k ($k = 0.83$) is the instrumental constant, λ denotes the wavelength of X-ray radiation in nanometres, θ denotes the Bragg angle in radians and β denotes the FWHM in radians. The most fundamental feature of the solid-state structure is the unit cell volume (V).

The density of the prepared nanoparticles (ρ_x) is calculated using the relation

$$\rho_x = \frac{ZM}{N_A V} \text{ g/cm}^3, \tag{4}$$

where Z is the number of formula units in the unit cell ($Z = 1$), M is the molecular mass of the sample and N_A is Avogadro's number.

The microstrain of the prepared nanoparticles (ε) is calculated from the equation,

$$\varepsilon = \frac{1}{\sin \theta} \left[\frac{\lambda}{D} - \beta \cos \theta \right], \tag{5}$$

where β is the full-width at half-maximum of the (110) peak and D is the average grain size.

The length of the dislocation lines per unit volume of the crystal is called the dislocation density [44]. Dislocations are defects in crystals caused by incorrect lattice registration in the surface area of the crystal. Dislocations are not equilibrium

defects to explain their presence in the measured dislocation densities, unlike vacancies and interstitial atoms [45–47]. In this case, dislocation density (δ) is calculated using the relation [48].

$$\delta = \frac{1}{D^2},$$ (6)

where, δ is the dislocation density and D is the particle size (nm).

The following formula is used to determine the surface area of the nanoparticles [49]:

$$S = \frac{6}{\rho \cdot D} \text{ cm}^2/\text{g},$$ (7)

where S is the surface area, ρ is the density and D is the grain or crystallite size. All the calculated lattice parameters of the BaZrO₃ nanoparticles prepared for three F/O ratios were listed in Table 1.

TABLE 1. Calculated lattice parameters of BaZrO₃ nanoparticles

Parameters/sample	$F/O = 0.5$	$F/O = 1.0$	$F/O = 1.5$	Standard Values
Lattice constant (Å)	4.1778	4.1642	4.1757	4.19
Unit cell volume $V(\text{Å}^3)$	72.92	72.21	72.81	73.72
Crystallite size D (nm)	49	47	72	—
Density (ρ) g/cm³	6.296	6.357	6.304	6.22
Dislocation Density $(\times 10^{14})$ Lines/metre	4.21	4.5	1.9	—
Surface area $(S) \times 10^6$ cm²/g	19.56	20.02	13.16	—
Micro strain $(\varepsilon) \times 10^{-3}$	2.0	2.1	1.3	—

3. Results and discussion

3.1. X-ray diffraction (XRD) analysis

BaZrO₃ sample XRD patterns are displayed in Fig. 1. The sharp spikes indicated the crystallinity of the BaZrO₃ nanoparticles prepared for three F/O ratios.
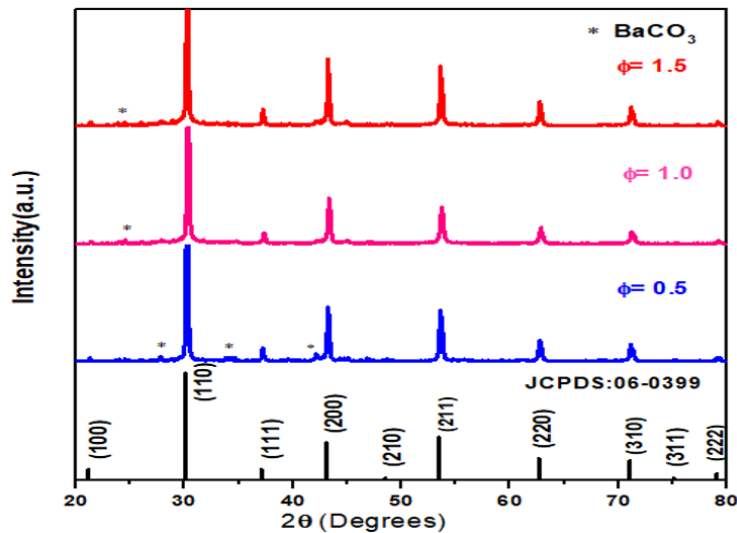
FIG. 1. The XRD pattern of BaZrO₃ samples prepared for three F/O ratios

These XRD patterns displayed seven main spikes of the BaZrO₃, such as (110), (111), (200), (210), (211), (220) and (310) well matched with cubic structure (JCPDS-06-0399). Very small amount of BaCO₃ (*) is presented at $2\theta = 24$, 28, 33, 42°. It is due to the dissolution of CO₂ from the air in the water. Mojdeh Azzizi et al. studied yttrium doped barium zirconate using two types of fuel with three different annealing temperatures 900, 1150 and 1300 °C. As a result,

citric acid fuel take lesser time for combustion and 1150 °C annealed sample produces an almost phase pure BAYZ nanopowder [50].

Table 1 illustrates that the calculated average lattice constants a, b and c values of BaZrO$_3$ nanoparticles suit the standard value. $F/O = 1.0$ gives a small crystallite size, its surface area is very high. $F/O = 1.5$ provides a very high crystallite size and very low dislocation density. FWHM (Full-width half maximum) value plays a major role in crystallite size. If the FWHM value increases, crystallite size should decrease. The unit cell volume and the density depend upon the lattice constant. The variation in the F/O ratio affects crystallite size. The release of additional gaseous products causes the crystallite size decreases by raising the F/O ratio from 0.5 to 1.0. High surface-to-volume ratio for grains decreases as excess heat is removed from the system [51]. The crystallite size increases from 41 to 63 with a further increase in the F/O ratio from 1.0 to 1.5. The increase in flame temperature of combustion that increases particle growth can be related to it [52]. The results indicated that the combustion-produced particle is nanocrystalline and has a size range of 47 – 72 nm.

3.2.   Rietveld analysis

Every type of crystalline material can be fitted with patterns using the Rietveld refining method, and it is highly efficient but not accessible for single crystals [53, 54]. The technique results in the use of the fact that the peak shape of Bragg reflections can be mathematically defined as well as the fluctuations in their width (FWHM) with the scattering angle 2θ. The Rietveld method enables least-squares refinement [χ^2 minimization] of an atomic model (crystal structure parameters) combined with a proper peak shape function, i.e., a simulated powder pattern, directly towards the observed powder pattern without extracting structure factor or integrated intensities once the structure is known and a suitable starting model is discovered. The Rietveld refinements for accurate structural parameters and the profile parameters start once the structural model is complete and the background contribution contains proper starting values. The resulting profile fit and the reliability factor or R-value values both show the refinement's progress. Up to the fit converges the structure has to be improved. In order to get accurately estimated standard deviations, which may be expressed quantitatively in terms of reliability factors or R-values, all parameters (profile and structural) must be refined simultaneously [55].

To get precise standard deviation values, Chi-square (χ^2) reduction was used to refine all structural parameters. Diffraction intensity data were taken into consideration for the computation of standard deviations. The intensity values are typically written as $I_{o,i}$, where 'o' stands for the observed values and 'i' for the intensity measured at 2-theta value $2\theta_i$. A model is fitted to the observed data in Rietveld analysis, and if the model is accurate, it will calculate the "true" intensity levels. The model-derived intensity values will be denoted as $I_{c,i}$, where 'c' stands for the computed model. The Rietveld algorithm optimizes the model function to minimize the weighted sum of squared differences between the observed and computed intensity values, i.e., to minimize $\sum_{i} w_i[I_{c,i} - I_{o,i}]^2$, where the weight, labeled as w_i, is $1/\sigma^2[I_{o,i}]$ [55] and the expected value of $\sum_{i} w_i[I_{c,i} - I_{o,i}]^2$ is one. This "best possible R_{wp}" quantity is a very useful concept and is called the expected R factor (R_{exp}):

$$R_{wp} = 100 \left[\frac{\sum_{i=1,n} w_i \left| I_i - I_{c,i} \right|^2}{\sum_{i=1,n} w_i I_i^2} \right]^{1/2}. \tag{8}$$

The actual R_{wp} should aim to be close to the statistically expected R value, R_{exp}:

$$R_{wp} = 100 \left[\frac{n - p}{\sum_{i=1,n} w_i I_i^2} \right]^{1/2}, \tag{9}$$

where n is the number of observations and p is the number of parameters. R_{exp} reflects the quality of data. Thus, the ratio between the R_{wp} and R_{exp} gives one the result of goodness of fit,

$$\chi^2 = \left[\frac{R_{wp}}{R_{exp}} \right]^2. \tag{10}$$

The refined BaZrO$_3$ diffraction pattern is displayed in Fig. 2. It is the result of using various F/O ratios followed by the EXPO programme. The plots make it very clear that the fitting accuracy is excellent. The calculated patterns are displayed in the same field as a dense line curve. The bottom field displays the variation between the calculated and observed intensity.

The cubic structure of the BaZrO$_3$ ceramic has a space group (Pm$\bar{3}$m) and point-group symmetry (O$_h$). Furthermore, Zirconium (Zr) atoms produce [ZrO$_6$] clusters with six oxygen (O) atoms, whereas Barium (Ba) atoms (lattice modifiers) make [BaO$_{12}$] clusters with twelve O atoms in a Cuboctahedral shape. Zr atoms are positioned Centro-symmetrically within the octahedron in [ZrO$_6$] clusters [56].

Table 2 contains the results for the lattice parameter, crystallite size, S, χ^2 and R-values.
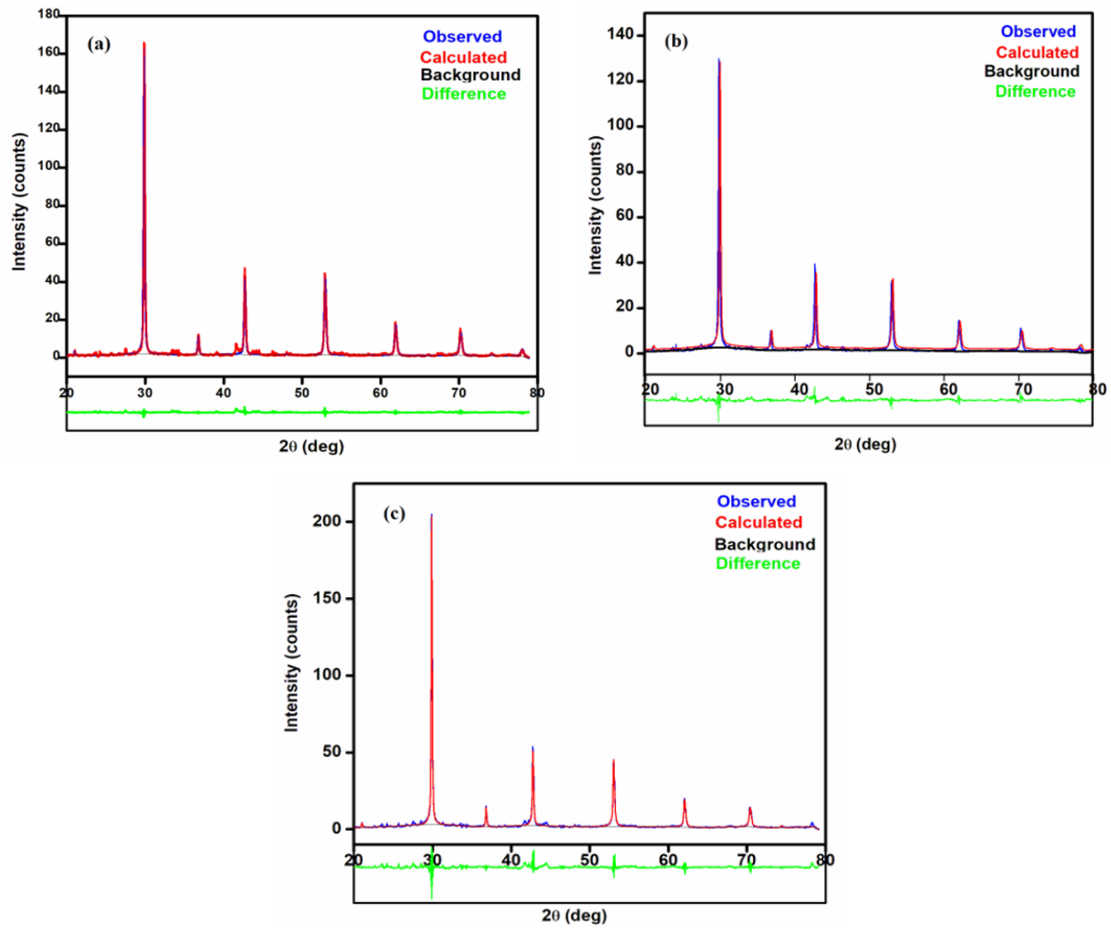
FIG. 2. Rietveld refinement output of the BaZrO$_3$ samples for three various F/O ratios: (a) $\varphi = 0.5$, (b) $\varphi = 1.0$, (c) $\varphi = 1.5$

TABLE 2. Rietveld refined data of BaZrO$_3$ nanoparticles

BaZrO$_3$	Lattice Parameters	Crystallite size (nm)	Micro strain (%) ($\times 10^{-3}$)	Rietveld Refine Parameters
$\Phi = 0.5$	$a = b = c = 4.18$ Å $\alpha = \beta = \gamma = 90°$	49.32	0.357	$R_{wp} = 18.69$ $R_p = 12.84$ $R_e = 14.53$ $S = 1.29$
$\Phi = 1.0$	$A = b = c = 4.17$ Å $\alpha = \beta = \gamma = 90°$	42.73	0.547	$R_{wp} = 16.050$ $R_p = 11.452$ $R_e = 12.38$ $S = 1.30$
$\Phi = 1.5$	$a = b = c = 4.18$ Å $\alpha = \beta = \gamma = 90°$	58.41	0.129	$R_{wp} = 16.98$ $R_p = 12.57$ $R_e = 14.92$ $S = 1.14$

On comparing the results of crystallite size with the XRD result, after the Rietveld refinement the crystallite size decreases then increases and the microstrain is increased then decreased. It is happened because of the rise in temperature. In the range of 1.14 to 1.30, the fitted pattern's goodness of fit (GoF) values can be found.

3.3. Raman spectroscopy analysis

The Raman spectra of $BaZrO_3$ are shown in Fig. 3. Although the perfect cubic perovskite would be expected to exhibit, all samples showed evidence of numerous vibrational modes. Second-order scattering was responsible for the identification of active vibrational modes in barium zirconate with oxygen vacancies [57, 58]. However, since the band at 200 cm^{-1} is connected to the torsional motion of the lattice, Karlsson et al. hypothesized that the spectrum comes from lattice distortions [59].
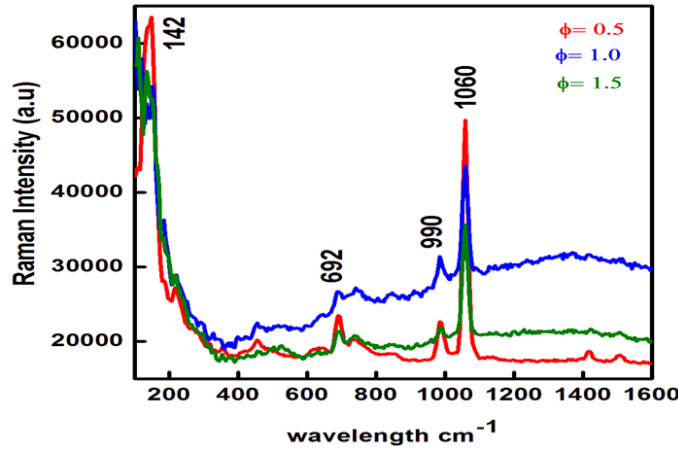
FIG. 3. FT RAMAN spectra of $BaZrO_3$ samples prepared for different F/O ratios

It is well known that $BaZrO_3$ with acceptor impurities, such as trivalent ions, leads to the formation of oxygen vacancies according to:

$$M_2O_2 \longrightarrow 2M'_{zr} + V_o^{\bullet\bullet} + 3O_o^X, \tag{11}$$

where M is the trivalent ion, V_{rmo} is the oxygen vacancy, and $3O_o^X$ is the oxygen at oxygen site. Hereafter the Kröger-Vink notation is used for point defects. Nominally pure $BaZrO_3$ may still contain intrinsic acceptor impurities in the form of Ba-vacancies which naturally occur during sintering at high temperatures due to loss of Ba. When exposed to humid atmosphere, the incorporation of protons occurs in the form of hydroxyl group (OH$^-$) that fills up the oxygen vacancies according to [60, 61]:

$$H_2O + O_o^X + V_o^{\bullet\bullet} \longleftrightarrow 2OH_o^{\bullet}. \tag{12}$$

From Eq. (12), the two OH$^-$ groups form after the reaction between water molecules and an oxygen vacancy.

Slodczyk et al. proposed that the active BZ Raman spectra are indicative of nano-domains with local symmetry that differs from that of the cubic structure, given the reality that the spectra include large bands and these distortions are supposed to be very minor [62, 63]. In simple terms, the majority of the bands are liked across all samples, only with some strength shifts or differences depending on composition. The translation oscillation modes from 50 to 250 cm^{-1} are produced by the motions of the Ba^{2+} network, which are dominated by the Coulomb interactions [62, 63].

While the peaks at higher frequencies indicate the modes of more covalently bonded oxygen octahedra, the peaks between 600 and 900 cm^{-1} are explained by the symmetric stretching (V) of oxygen bonds [62–64]. Furthermore, the $BaCO_3$ vibrational peak with the Raman shift of 1060 cm^{-1} indicates the creation of carbonate (CO_3) species [65].

3.4. UV-vis spectroscopy analysis

The UV-Vis absorbance spectrum of $BaZrO_3$ ceramics is shown in Fig. 4. The peak around 220 nm can be attributed to ban edge absorption of $BaZrO_3$. According to the method outlined by Wood and Tauc [66], the optical band gap energy (E_{gap}) was calculated using the following equation:

$$(\alpha h\nu) = B\left(h\nu - E_{gap}\right)^n, \tag{13}$$

where B is a band tailoring constant, n is a constant related to the various types of electronic transitions ($n = 1/2$, 2, $3/2$ or 3) for direct allowed, indirect allowed, direct forbidden, and indirect forbidden transitions, respectively [67], h is the Plank constant, ν is the frequency, E_{gap} is the optical band gap, and α is absorbance. In this instance, the indirect acceptable transition one is taken to be $n = 2$.

The Tauc plot of $BaZrO_3$ is shown in Fig. 5. for three F/O ratios ($\varphi = 0.5$, 1.0 and 1.5). The band gap of the material, if it is a direct transition, as shown by the Tauc plots [68], is obtained by extrapolating the linear component of
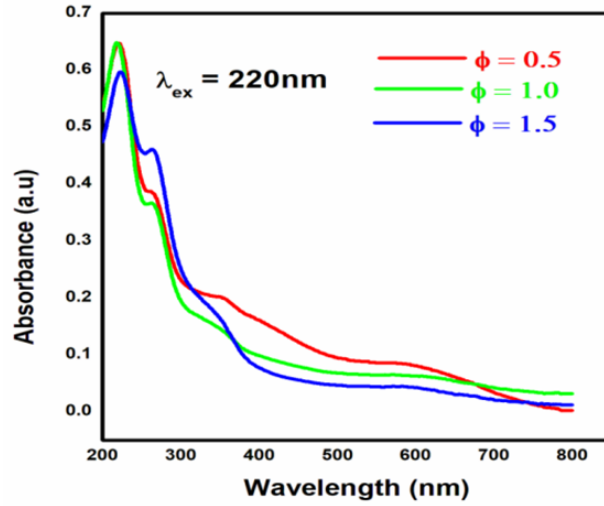
FIG. 4. UV-Vis absorbance spectra of BaZrO$_3$ samples prepared for different F/O ratios

$(\alpha h\nu)^2$ versus (hc/λ), to obtain the E_{gap} values. For the respective F/O ratios of 0.5, 1.0, and 1.5, the band gap of pure BaZrO$_3$ at room temperature is determined to be 2.02, 2.96, and 3.09 eV. The excitation wavelength is 220 nm. As the fuel content rises, the bandgap of BaZrO$_3$ increases.
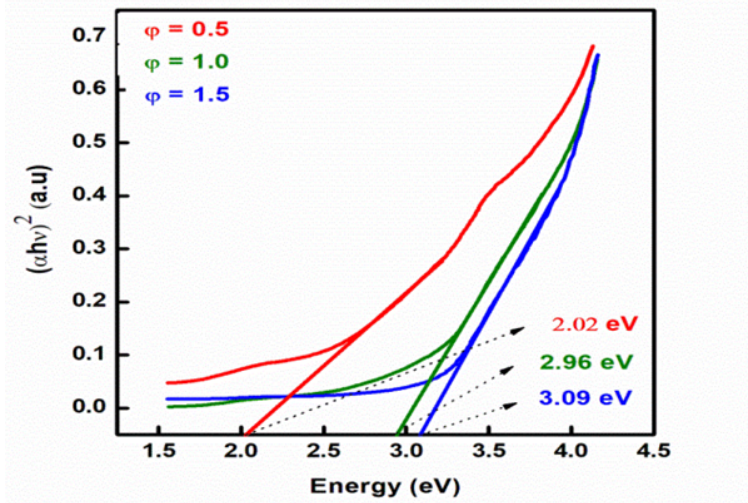
FIG. 5. Tauc plot of BaZrO$_3$ samples prepared for different F/O ratios

3.5. Impedance spectroscopy analysis

The electrical and dielectric properties of a polycrystalline BaZrO$_3$ ceramic and their interfaces with electronically conducting electrodes have been examined in a wide range of frequencies (100 Hz – 1 MHz) at room temperature using the complex impedance spectroscopy method [69]. The complex dielectric permittivity, abbreviated ε^*, complex impedance, abbreviated Z^*, and electric modulus, abbreviated M^*, which are connected to one another as follows:

$$Z^* = Z' + jZ'', \tag{14}$$

$$M^* = \frac{1}{\varepsilon^*\omega}, \tag{15}$$

$$\frac{1}{\varepsilon^*\omega} = j\left(\omega C_0\right)Z^*, \tag{16}$$

$$j(\omega C_0)Z^* = M' + jM'', \tag{17}$$

where (Z', M') and (Z'', M'') are the real and imaginary compounds of impedance and modulus, respectively, $j = \sqrt{-1}$ is the imaginary factor and ω is the angular frequency,

$$\omega = 2\pi f. \tag{18}$$

There are two parts to the impedance expression: a real part and an imaginary part. A "Nyquist Plot" is created when the real part (Z_{real}) is plotted on the X-axis and the imaginary part (Z_{imag}) is plotted on the Y-axis (see Fig. 6). The Z_{imag} is negative, whereas each point on the Nyquist plot represents an impedance value at a certain frequency point. Low frequency impedance is applied to the right side of the plot along the X-axis, and higher frequency impedances are applied to the left. Additionally, impedance can be shown as a vector (arrow) with a length of $|Z|$ on a Nyquist plot. The "phase angle" is the angle formed by this arrow and the X-axis [70]. A Bode plot is widely used in the engineering community compared to the Nyquist plot. It consists of two different logarithmic plots: frequency vs magnitude and frequency vs phase (Fig. 7). It is another technique to describe the impedance results.
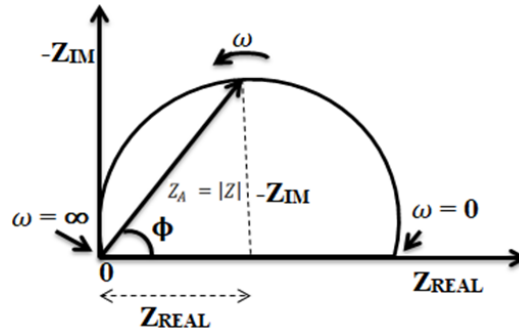
FIG. 6. Nyquist plot with impedance vector
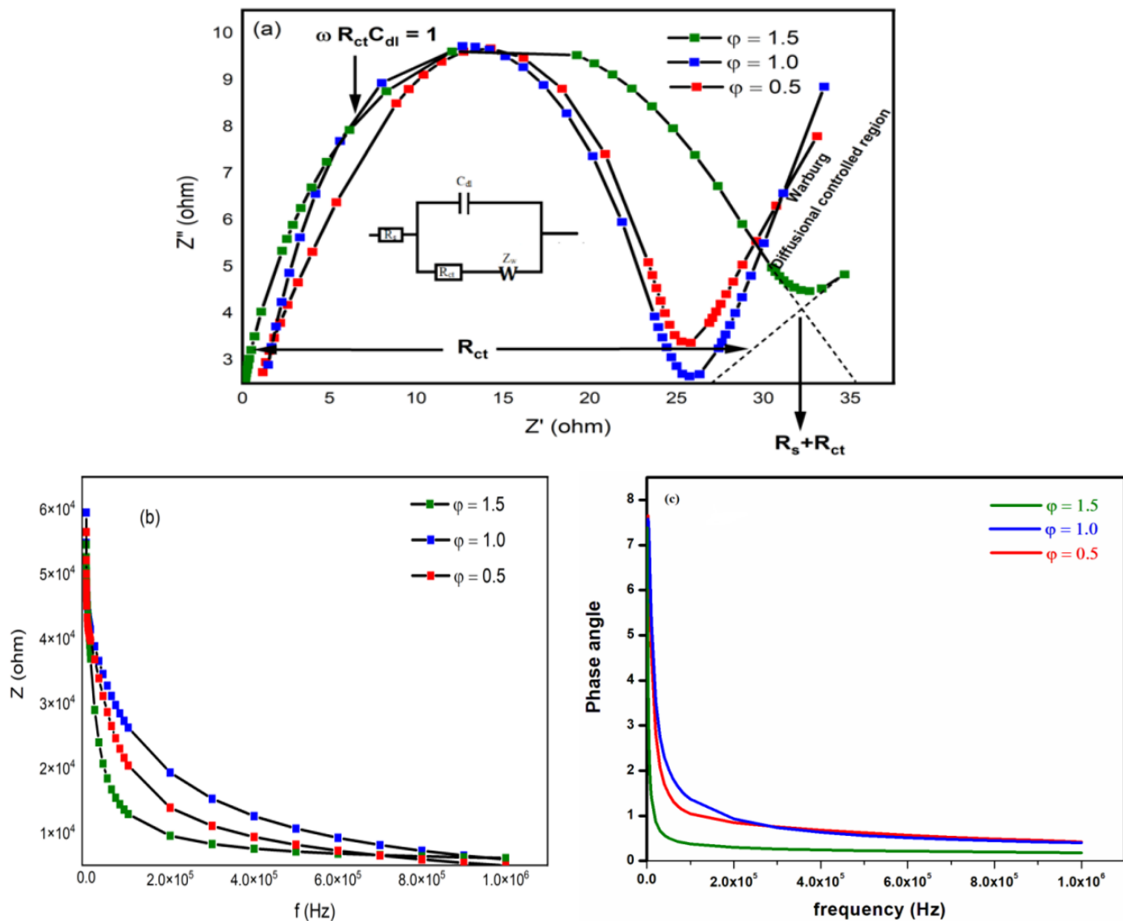
FIG. 7. (a) Nyquist plot for $BaZrO_3$ with $\varphi = 0.5$, 1.0 and 1.5 at room temperature; (b) frequency vs magnitude (Bode plot); (c) frequency vs phase angle (Bode plot) for $BaZrO_3$ with $\varphi = 0.5$, 1.0 and 1.5 at room temperature

Impedance is really measured by introducing a potential wave to the working electrode and monitoring the ensuing current wave Z. Z_{real}, and Z_{imag} are taken from these two waves and sketched. These parameters are measured for potential waves with various frequencies to produce the spectrum. In a three-electrode system, an EIS experiment is carried out by fixing an applied voltage [71], according to the initial report on electrochemical impedance spectroscopy that was published in 1975 [72]. The generated Warburg impedance (W), charge transfer resistance (R_{ct}), and solution resistance (R_s) are gathered and shown in the Nyquist plots.

The Warburg impedance (W) is an extra resistance that can be produced by the diffusion of molecules or redox species. Frequency affects the manner in which this impedance behaves. In fact, the diffusing reactants do not have to go very far. The Warburg impedance is minimal at high frequencies. The force to diffuse the redox molecules increases the Warburg resistance at low frequencies. The Nyquist plot shows the infinite Warburg impedance as a tilted line with a 45° slope. On the Bode plot, however, the Warburg effect appears as a 45° phase shift.

The Nyquist curve of BaZrO₃ with $\varphi = 0.5$, 1.0, and 1.5 at room temperature is shown in Fig. 7(a). Warburg resistance, which is induced by the frequency dependence of ion diffusion from the electrolyte to the surface, is a phenomenon as all samples exhibit a circular arc in the high-frequency zone and nearly a straight line in the low-frequency region. As the F/O ratio increases, the semicircle's diameter gradually changes. A Bode curve of the impedance $Z(\Omega)$ for BaZrO₃ is shown in Fig. 7(b). A Bode plot of the phase angle for BaZrO₃ is shown in Fig. 7(c). For $\varphi = 0.5$, 1.0, and 1.5 ratios, the impedance magnitude $|Z|$ reduces with increasing F/O ratio at low frequency and decreases at high frequency. For observing phase margins where the system becomes unstable (violent phase or magnitude changes), the Bode plot offers many advantages. The study of sensors, filters, and transistors in electronic devices can benefit from it as a result [73]. Real and imaginary part of impedance increases with increasing F/O ratio.

Ionic conductivity is reduced by 4.833×10^{-3} to 3.327×10^{-3}. It introduces significant structural defects to the BaZrO₃ crystal, as evidence by large lattice microstrain. In general, the Oxygen vacancy assisted high ionic conductivity [74].

Bulk resistance of the three various F/O ratio value, the calculated value of ionic conductivity were listed in Table 3.

TABLE 3. Ionic conductivity data of BaZrO₃ electrolyte

Sample	Sample thickness (cm)	Bulk resistance (Ω)	Area of the sample (cm)	Ionic conductivity S/cm
$\varphi = 0.5$	0.1901	25.54	1.54	4.833×10^{-3}
$\varphi = 1.0$	0.1762	25.91	1.54	4.416×10^{-3}
$\varphi = 1.5$	0.1661	32.42	1.54	3.327×10^{-3}

The ionic conductivity was found to be

$$\sigma = \frac{L}{R_b^* A}, \tag{19}$$

where L is the thickness (cm), A is the contact area (cm²), and R_b (Ω) is the bulk resistance of the BaZrO₃ electrolyte, σ is the ionic conductivity (S·cm⁻¹). The Nyquist plot of the complex impedance readings was used to calculate R_b. The Ionic conductivity result shows the BaZrO₃ electrolyte material can be used as semiconducting device application.

The EIS approach, a non-destructive investigation tool, can be used to efficiently characterize physical and chemical processes in fuel cells as well as energy storage devices. In order to monitor these materials' and devices' performance and stability, as well as their charge transport characteristics, the EIS can be used [75].

Figure 8 displays the impedances of BaZrO₃ at room temperature. For $\varphi = 0.5$, 1.0, and 1.5 ratios, the real component $Z'(f)$ of impedance decreases with increasing frequency (Fig. 8(a)). The imaginary portion $Z''(f)$ of BaZrO₃ is shown in Fig. 8(b), and it increases to a maximum value before it starts to decrease at high frequencies, demonstrating the presence of a relaxation process in the system. The relaxation period for the dielectric-relaxation process is provided by the Z'' peak.

4. Conclusion

The sol-gel auto-combusted method was used to successfully synthesise perovskite Barium Zirconate nanoparticles with various F/O ratios. XRD was used to examine the crystalline size. The Rietveld refinement verified that the BaZrO₃ phase was unique and clear. Raman spectroscopy was used to confirm the existence of various modes. With an increasing F/O ratio, it was discovered that the optical band gap increases from 2.02 to 3.09 eV. As the F/O ratio increased, the impedance and relaxation time of a BaZrO₃ pellet for impedance spectroscopy decreased. For various F/O ratios (for $\varphi = 0.5$, 1.0, and 1.5), the BaZrO₃ electrolyte's ionic conductivity ranged from 3.327×10^{-3} to 4.833×10^{-3}. BaZrO₃ nanoparticles can be used for the development of energy storage devices due to good electrical properties and high ionic conductivity.
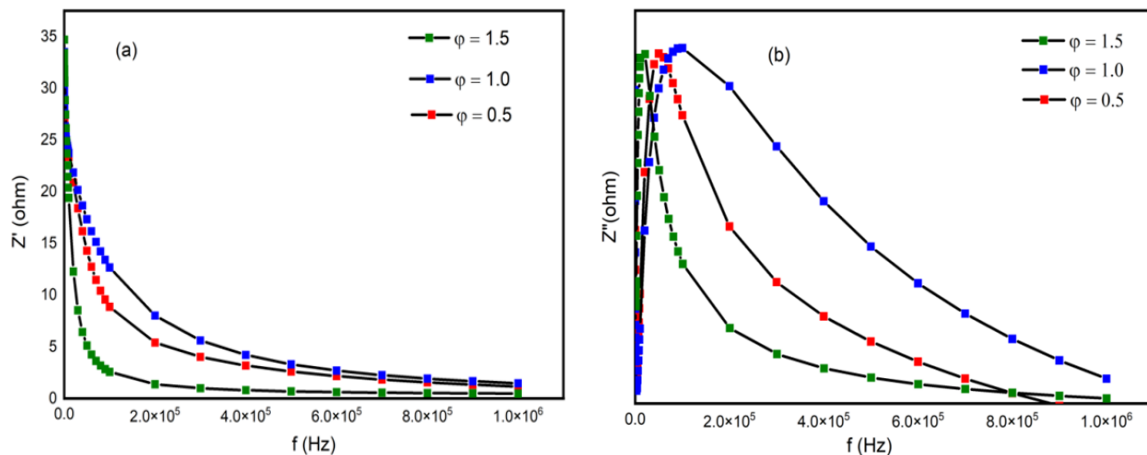
FIG. 8. (a) Real part and (b) imaginary part of impedance as a function of frequency (Bode plot) for BaZrO$_3$ with $\varphi = 0.5$, 1.0 and 1.5 at room temperature

References

[1] Norton F.H. *Fine ceramics: technology and applications*. McGraw-Hill, New York, 1970.

[2] Boschini F., Rulmont A., Cloots R., Moreno, R. Rheological behaviour of BaZrO$_3$ suspensions in non-aqueous media. *Ceramics International*, 2009, **35** (3), P. 1007–1013.

[3] Huang J., Zhou L., Wang Z., Lan Y., Tong Z., Gong F., Li, L. Photoluminescence properties of SrZrO$_3$: Eu^{3+} and BaZrO$_3$: Eu^{3+} phosphors with perovskite structure. *J. of Alloys and Compounds*, 2009, **487** (1–2), L5–L7.

[4] Iwahara H., Asakura Y., Katahira K., Tanaka, M. Prospect of hydrogen technology using proton-conducting ceramics. *Solid State Ionics*, 2004, **168** (3–4), P. 299–310.

[5] Kreuer K.D. Aspects of the formation and mobility of protonic charge carriers and the stability of perovskite-type oxides. *Solid State Ionics*, 1999, **125** (1–4), P. 285–302.

[6] Zhou H., Mao Y., Wong S.S. Shape control and spectroscopy of crystalline BaZrO$_3$ perovskite particles. *J. of Materials Chemistry*, 2007, **17** (17), P. 1707–1713.

[7] Dong Z., Ye T., Zhao Y., Yu J., Wang F., Zhang L., Guo S. Perovskite BaZrO$_3$ hollow micro- and nanospheres: controllable fabrication, photoluminescence and adsorption of reactive dyes. *J. of Materials Chemistry*, 2011, **21** (16), P. 5978–5984.

[8] Cavalcante L.S., Sczancoski J.C., Espinosa J.W.M., Mastelaro V.R., Michalowicz A., Pizani P.S., Longo E. Intense blue and green photoluminescence emissions at room temperature in barium zirconate powders. *J. of Alloys and Compounds*, 2009, **471** (1–2), P. 253–258.

[9] Parida S., Rout S.K., Cavalcante L.S., Sinha E., Li M.S., Subramanian V., Longo E. Structural refinement, optical and microwave dielectric properties of BaZrO$_3$. *Ceramics International*, 2012, **38** (3), P. 2129–2138.

[10] Choudhury P.R., Krupanidhi S.B. Dielectric response of BaZrO$_3$/BaTiO$_3$ and SrTiO$_3$/BaZrO$_3$ superlattices. *J. of Applied Physics*, 2008, **104** (11), 114105.

[11] Moreira M.L., Gurgel M.F.C., Mambrini G.P., Leite E.R., Pizani P.S., Varela J.A., Longo E. Photoluminescence of barium titanate and barium zirconate in multilayer disordered thin films at room temperature. *The J. of Physical Chemistry A*, 2008, **112** (38), P. 8938–8942.

[12] Jia X., Fan H., Lou X., Xu J. Synthesis and gas sensing properties of perovskite CdSnO$_3$ nanoparticles. *Applied Physics A*, 2009, **94**, P. 837–841.

[13] LoPinto D.E. *Tunable Piezoelectric Transducers via Custom 3D Printing: Conceptualization, Creation, and Customer Discovery of Acoustic Applications*. Virginia Tech, 2021.

[14] Yamanaka S., Kurosaki K., Maekawa T., Matsuda T., Kobayashi S.I., Uno M. Thermochemical and thermophysical properties of alkaline-earth perovskites. *J. of Nuclear Materials*, 2005, **344** (1-3), P. 61–66.

[15] Shirpour M., Rahmati B., Sigle W., van Aken P.A., Merkle, R., Maier J. Dopant segregation and space charge effects in proton-conducting BaZrO$_3$ perovskites. *The J. of Physical Chemistry C*, 2012, **116** (3), P. 2453–2461.

[16] Herbert J.M. *Ceramic dielectrics and Capacitors*, 1985, Vol. 6, Philadelphia.

[17] Sundell P.G., Björketun M.E., Wahnström G. Thermodynamics of doping and vacancy formation in BaZrO$_3$ perovskite oxide from density functional calculations. *Physical Review B*, 2006, **73** (10), 104112.

[18] Dhahri K., Bejar M., Dhahri E., Soares M. J., Graça M.F.P., Sousa M.A., Valente M.A. Blue-green photoluminescence in BaZrO$_{3-\delta}$ powders. *Chemical Physics Letters*, 2014, **610**, P. 341–344.

[19] Wan Ali W.F.F., Rejab N.A., Othman M., Ain M.F., Ahmad Z.A. An investigation of dielectric resonator antenna produced from silicon (100) enhanced by strontium doped-barium zirconate films. *J. of sol-gel science and technology*, 2012, **61**, P. 411–420.

[20] Park J.S., Lee J.H., Lee H.W., Kim B.K. Low temperature sintering of BaZrO$_3$-based proton conductors for intermediate temperature solid oxide fuel cells. *Solid State Ionics*, 2010, **181** (3–4), P. 163–167.

[21] Cullity B.D. *Elements of X-ray Diffraction*, Addison-Wesley Publishing, 1956.

[22] Kittel C., McEuen P. *Introduction to solid state physics*, John Wiley & Sons, 2018.

[23] Patil K.C., Aruna S.T., Ekambaram S. Combustion synthesis. *Current opinion in solid state and materials science*, 1997, **2** (2), P. 158–165.

[24] Jain S.R., Adiga K.C., Verneker V.P. A new approach to thermochemical calculations of condensed fuel-oxidizer mixtures. *Combustion and flame*, 1981, **40**, P. 71–79.

[25] Hwang C.C., Huang T.H., Tsai J.S., Lin C.S., Peng C.H. Combustion synthesis of nanocrystalline ceria (CeO$_2$) powders by a dry route. *Materials Science and Engineering: B*, 2006, **132** (3), P. 229–238.

[26] Mukasyan A.S., Epstein P., Dinka, P. Solution combustion synthesis of nanomaterials. *Proceedings of the combustion institute*, 2007, **31** (2), P. 1789–1795.

[27] Tyagi A.K., Chavan S.V., Purohit R.D. Visit to the fascinating world of nano-ceramic powders via solution-combustion. *Indian J. of Pure & Applied Physics*, 2006, **44** (2), P. 113–118.

[28] Chen W., Li F., Yu J., Liu L. A facile and novel route to high surface area ceria-based nanopowders by salt-assisted solution combustion synthesis. *Materials Science and Engineering: B*, 2006, **133** (1–3), P. 151–156.

[29] Bedekar V., Grover V., Nair S., Purohit R.D., Tyagi A. K. Nanocrystalline electroceramics by combustion method. *Synthesis and Reactivity in Inorganic, Metal-Organic and Nano-Metal Chemistry*, 2007, **37** (5), P. 321–326.

[30] Xu Q., Huang D.P., Chen W., Lee J.H., Wang H., Yuan R.Z. Citrate method synthesis, characterization and mixed electronic–ionic conduction properties of $La_{0.6}Sr_{0.4}Co_{0.8}Fe_{0.2}O_3$ perovskite-type complex oxides. *Scripta Materialia*, 2004, **50** (1), P. 165–170.

[31] Majid A., Tunney J., Argue S., Wang D., Post M., Margeson J. Preparation of SrFeO∼2.85 perovskite using a citric acid assisted Pechini-type method. *J. of alloys and compounds*, 2005, **398** (1–2), P. 48–54.

[32] Palmisano P., Russo N., Fino P., Fino D., Badini C. High catalytic activity of SCS-synthesized ceria towards diesel soot combustion. *Applied Catalysis B: Environmental*, 2006, **69** (1–2), P. 85–92.

[33] Carvalho M., Costa F.A., Pereira I.S., Bassat J., Grenier J. New preparation method of $La_{n+1}Ni_nO_{3n+1-\delta}$ ($n = 2, 3$). *J. of Materials Chemistry*, 1997, **7** (10), P. 2107–2111.

[34] Marinšek M., Zupan K., Maeek J. Ni–YSZ cermet anodes prepared by citrate/nitrate combustion synthesis. *J. of power sources*, 2002, **106** (1–2), P. 178–188.

[35] Chakroborty A., Sharma A.D., Maiti B., Maiti H.S. Preparation of low-temperature sinterable $BaCe_{0.8}Sm_{0.2}O_3$ powder by autoignition technique. *Materials letters*, 2002, **57** (4), P. 862–867.

[36] Mali A., Ataie A. Influence of the metal nitrates to citric acid molar ratio on the combustion process and phase constitution of barium hexaferrite particles prepared by sol-gel combustion method. *Ceramics International*, 2004, **30** (7), P. 1979–1983.

[37] Hernandez T., Bautista M.C. The role of the synthesis route to obtain densified TiO₂-doped alumina ceramics. *J. of the European Ceramic Society*, 2005, **25** (5), P. 663–672.

[38] Pechini M.P. US Patent No. 3330697, 1967, July.

[39] Epifani M., Melissano E., Pace G., Schioppa M. Precursors for the combustion synthesis of metal oxides from the sol-gel processing of metal complexes. *J. of the european ceramic society*, 2007, **27** (1), P. 115–123.

[40] Wang P.J., Zhou D., Li J., Pang L.X., Liu W.F., Su J.Z., Trukhanov A. Significantly enhanced electrostatic energy storage performance of P(VDF-HFP)/BaTiO₃–Bi(Li$_{0.5}$Nb$_{0.5}$)O₃ nanocomposites. *Nano Energy*, 2020, **78**, 105247.

[41] Trukhanov S.V., Trukhanov A.V., Turchenko V.A., Trukhanov A.V., Trukhanova E.L., Tishkevich D.I., Gudkova S.A. Polarization origin and iron positions in indium doped barium hexaferrites. *Ceramics International*, 2018, **44** (1), P. 290–300.

[42] Kumar D., Singh B. BaZrO₃ and Cs-BaZrO₃ catalysed transesterification of Millettia Pinnata oil and optimisation of reaction variables by response surface Box-Behnken design. *Renewable Energy*, 2019, **133**, P. 411–421.

[43] Borja-Urby R., Díaz-Torres L.A., Salas P., Moctezuma E., Vega M., Ángeles-Chávez C. Structural study, photoluminescence, and photocatalytic activity of semiconducting BaZrO₃: Bi nanocrystals. *Materials Science and Engineering: B*, 2011, **176** (17), P. 1382–1387.

[44] Nehru L.C., Swaminathan V., Sanjeeviraja C. Photoluminescence studies on nanocrystalline tin oxide powder for optoelectronic devices. *American J. of Materials Science*, 2012, **2** (2), P. 6–10.

[45] Beltrán A., Andrés J., Longo E., Leite E.R. Thermodynamic argument about SnO₂ nanoribbon growth. *Applied physics letters*, 2003, **83** (4), P. 635–637.

[46] Schmalzried H., Kröger F.A. *The Chemistry of Imperfect Crystals*, North-Holland Publishing Company, Amsterdam, 1964.

[47] Bedir M., Öztaş M., Bakkaloğlu Ö.F., Ormanci R. Investigations on structural, optical and electrical parameters of spray deposited ZnSe thin films with different substrate temperature. *The European Physical J. B-Condensed Matter and Complex Systems*, 2005, **45**, P. 465–471.

[48] Dhanam M., Balasundaraprabhu R., Jayakumar S., Gopalakrishnan P., Kannan M.D. Preparation and study of structural and optical properties of chemical bath deposited copper indium diselenide thin films. *Physica Status Solidi A*, 2002, **191** (1), P. 149–160.

[49] Park J.Y., Lee Y.J., Jun K.W., Baeg J.O., Yim, D.J. Chemical synthesis and characterization of highly oil dispersed MgO nanoparticles. *J. of Industrial and engineering chemistry*, 2006, **12** (6), P. 882–887.

[50] Azizi M., Paydar M.H., Alafzadeh M. Influence of the Calcination Temperature and Fuel Composition on Synthesis of $BaZr_{0.8}Y_{0.2}O_{3-\delta}$ by Solution Combustion Method for High Proton conductivity. *Int. J. of Advanced Science and Technology*, 2016, **96**, P. 11–20.

[51] Elilarassi R., Chandrasekaran G. Synthesis and optical properties of Ni-doped zinc oxide nanoparticles for optoelectronic applications. *Optoelectronics Letters*, 2010, **6** (1), P. 6–10.

[52] Toniolo J., Takimi A.S., Andrade M.J., Bonadiman R., Bergmann C.P. Synthesis by the solution combustion process and magnetic properties of iron oxide (Fe₃O₄ and α-Fe₂O₃) particles. *J. of Materials Science*, 2007, **42**, P. 4785–4791.

[53] Rietveld H.M. A profile refinement method for nuclear and magnetic structures. *J. of applied Crystallography*, 1969, **2** (2), P. 65–71.

[54] Rietveld H.M. Line profiles of neutron powder-diffraction peaks for structure refinement. *Acta Crystallographica*, 1967, **22** (1), P. 151–152.

[55] Young R.A. The Rietveld method. *Int. Union of Crystallography*, 1993, **5**, P. 1–38.

[56] Sczancoski J.C., Cavalcante L.S., Badapanda T., Rout S.K., Panigrahi S., Mastelaro, V.R., Longo E. Structure and optical properties of [Ba$_{1-x}$Y$_{2x/3}$](Zr$_{0.25}$Ti$_{0.75}$)O₃ powders. *Solid State Sciences*, 2010, **12** (7), P. 1160–1167.

[57] Schaufele R.F., Weber M.J. First- and second-order Raman scattering of SrTiO₃. *The J. of Chemical Physics*, 1967, **46** (7), P. 2859–2861.

[58] Charrier-Cougoulic I., Pagnier T., Lucazeau G. Raman spectroscopy of perovskite-type BaCe$_x$Zr$_{1-x}$O₃ ($0 \leq x \leq 1$). *J. of Solid State Chemistry*, 1999, **142** (1), P. 220–227.

[59] Karlsson M., Matic A., Knee C.S., Ahmed I., Eriksson S.G., Börjesson L. Short-Range Structure of Proton-Conducting Perovskite BaIn$_x$Zr$_{1-x}$O$_{3-x/2}$ ($x = 0$–0.75). *Chemistry of Materials*, 2008, **20** (10), P. 3480–3486.

[60] Kreuer K. On the development of proton conducting materials for technological applications. *Solid State Ionics*, 1997, **97** (1–4), P. 1–15.

[61] Norby T., Larring Y. Concentration and transport of protons in oxides. *Current Opinion in Solid State and Materials Science*, 1997, **2** (5), P. 593–599.

[62] Karlsson M., Ahmed I., Matic A., Eriksson S.G. Short-range structure of proton-conducting BaM$_{0.10}$Zr$_{0.90}$O$_{2.95}$ (M= Y, In, Sc and Ga) investigated with vibrational spectroscopy. *Solid State Ionics*, 2010, **181** (3–4), P. 126–129.

[63] Slodczyk A., Colomban P., Willemin S., Lacroix O., Sala B. Indirect Raman identification of the proton insertion in the high-temperature [Ba/Sr][Zr/Ti]O₃-modified perovskite protonic conductors. *J. of Raman Spectroscopy: An Int. J. for Original Work in all Aspects of Raman Spectroscopy, Including Higher Order Processes, and also Brillouin and Rayleigh Scattering*, 2009, **40** (5), P. 513–521.

[64] Slodczyk A., Limage M. H., Colomban P., Zaafrani O., Grasset F., Loricourt J., Sala B. Substitution and proton doping effect on SrZrO₃ behaviour: High-pressure raman study. *J. of Raman Spectroscopy*, 2011, **42** (12), P. 2089–2099.

[65] Li X., Liu M., Lai S.Y., Ding, D., Gong, M., Lee J.P., Liu M. In situ probing of the mechanisms of coking resistance on catalyst-modified anodes for solid oxide fuel cells. *Chemistry of Materials*, 2015, **27** (3), P. 822–828.

[66] Wood D.L., Tauc J.S. Weak absorption tails in amorphous semiconductors. *Physical Review B*, 1972, **5** (8), 3144.

[67] Badapanda T., Rout S.K., Cavalcante L.S., Sczancoski J.C., Panigrahi S., Longo E., Li M.S. Optical and dielectric relaxor behaviour of Ba(Zr$_{0.25}$Ti$_{0.75}$)O$_3$ ceramic explained by means of distorted clusters. *J. of Physics D: Applied Physics*, 2009, **42** (17), 175414.

[68] Turton R., Turton R.J. *The quantum dot: A journey into the future of microelectronics*. Oxford University Press, USA, 1996.

[69] Macdonald J.R. Impedance spectroscopy: Models, data fitting, and analysis. *Solid state ionics*, 2005, **176** (25–28), P. 1961–1969.

[70] Lvovich V.F. Electrochemical Impedance Spectroscopy (EIS) applications to sensors and diagnostics. *Encyclopedia of Applied Electrochemistry*, Eds.: Kreysa G., Ota K.-i., Savinell R.F., 2014, P. 485–507.

[71] Orazem M.E., Tribollet B. Electrochemical impedance spectroscopy. *New Jersey*, 2008, **1**, P. 383–389.

[72] Ha L.D., Park K., Chang B.Y., Hwang S. Implementation of second-generation fourier transform electrochemical impedance spectroscopy with commercial potentiostat and application to time-resolved electrochemical impedance spectroscopy. *Analytical chemistry*, 2019, **91** (22), P. 14208–14213.

[73] Choi W., Shin H.C., Kim J.M., Choi J.Y., Yoon W.S. Modeling and applications of electrochemical impedance spectroscopy (EIS) for lithium-ion batteries. *J. of Electrochemical Science and Technology*, 2020, **11** (1), P. 1–13.

[74] Wu H., Li F. Oxygen vacancy-assisted high ionic conductivity in perovskite LaCoO$_{3-\delta}$ ($\delta = 1/3$) thin film: A first-principles-based study. *Physics Letters A*, 2019, **383** (2–3), P. 210–214.

[75] Cherian C.T., Zheng M., Reddy M.V., Chowdari B.V.R., Sow C.H. Zn$_2$SnO$_4$ nanowires versus nanoplates, electrochemical performance and morphological evolution during Li-cycling. *ACS Applied Materials and Interfaces*, 2013, **5** (13), P. 6054–6060.

Information about the authors:

J. Abimalar – Department of Physics and Research Centre, Scott Christian College (Autonomous), Nagercoil – 629003, Tamil Nadu, India; Manonmaniam Sundaranar University, Abishekapatti, Tirunelveli – 627012, Tamil Nadu, India; ORCID 0009-0006-5388-0816; University reg. no. 20213162132017; jabimalar98@gmail.com

V. Anslin Ferby – Department of Physics and Research Centre, Scott Christian College (Autonomous), Nagercoil – 629003, Tamil Nadu, India; Manonmaniam Sundaranar University, Abishekapatti, Tirunelveli – 627012, Tamil Nadu, India; ORCID 0000-0001-6298-1498; anslinv@gmail.com

Conflict of interest: the authors declare no conflict of interest.